PERFORMANCE AND LOADS PREDICTIONS OF A SLOWED UH-60A ROTOR AT HIGH ADVANCE RATIOS

Mark Potsdam mark.potsdam@us.army.mil
Hyeonsoo Yeo hyeonsoo.yeo@us.army.mil
Robert Ormiston robert.ormiston@us.army.mil
U.S. Army Aviation Development Directorate - Aeroflightdynamics Directorate (AMRDEC)
Research, Development, and Engineering Command, Moffett Field, CA, USA

ABSTRACT

The UH-60A slowed rotor wind tunnel test data represents a unique database for analysis validation of high advance ratio flight conditions. Rotorcraft comprehensive analysis (CAMRAD II, RCAS) using prescribed vortex wake models and coupled high-fidelity computational fluid dynamics (CFD) and computational structural dynamics (CSD) (Helios) have been performed, and comparisons are made for rotor performance and controls, airloads, and structural loads. The strength and weaknesses of the analyses are highlighted. All three analyses are in general agreement, although the CFD trend predictions as a function of collective or advance ratio are more satisfying. Normal force airloads are in good agreement with the data, while pitching moments show significant deviations, especially on the advancing side. Flap bending moment peak-to-peak and vibratory loads are captured accurately at all conditions, but only the torsion moments at high speed are in good agreement. Overall results indicate that structural load trends with increasing advance ratio or decreasing rotor RPM can be predicted by state-of-the-art rotorcraft analyses. The importance of blade root shank modeling at high advance ratio is shown. CFD directly models the shank geometry while comprehensive analyses require empirical correlation of the shank drag.

NOMENCLATURE

- a speed of sound
- A rotor area, πR^2
- c local chord
- C_D Rotor drag coefficient, $D/\rho(\Omega R)^2\pi R^2$
- c_x section x-force in-plane coefficient, $[FX]/ \frac{1}{2}\rho V_T^2 c$
- c_p pressure coefficient, $(p - p_\infty)/\frac{1}{2}\rho V_T^2$
- C_{Ptot} Total power coefficient, $P/\rho(\Omega R)^3 A$
  = profile power + induced power = $C_{Po} + C_{Pi}$
  = torque + drag power = $C_Q + \mu C_D$
- C_Q Torque coefficient, $Q/\rho(\Omega R)^2 AR$
- C_T Thrust coefficient, $T/\rho(\Omega R)^2 A$
- M^2c_n, M^2c_x, section normal force, x-force coefficient, $[NF,FX]/\frac{1}{2}\rho a^2 c$
- M^2c_m section pitching moment coefficient, $PM/\frac{1}{2}\rho a^2 c^2$
- M_{tip} hover tip Mach number
- NF, PM, FX dimensional airfoil section normal force, pitching moment, x-force (rotating hub system)
- p pressure
- r radial location
- R rotor radius, 26.83 ft
- V freestream velocity
- V_T local tangential velocity, $V\sin(\psi) + r\Omega$
- α_s shaft angle, deg (+ nose up)
- θ_0 collective angle, deg
- θ_{1c}, θ_{1s} lateral, longitudinal cyclic angles, deg
- μ advance ratio, $V/\Omega R$
- ρ density
- σ solidity, 0.0826
- ψ azimuth angle, deg
- Ω rotor rotation rate, rad/s (258 RPM nominal, 103 RPM slowed)

Presented at the 39th European Rotorcraft Forum, Moscow, Russia, September 2013.

INTRODUCTION

Emerging military and commercial needs are leading to requirements for significant increases in speed and range capabilities over what conventional helicopters can achieve. The desired performance attributes for a future vertical lift aircraft in the US Army [1] call for high speed (170-300 kts), extended range (> 400 km), high/hot performance (6K/95°F), and increased fuel efficiency. A key technology to meeting these goals efficiently with an edgewise rotor is most likely a slowed rotor configuration. Conventional helicopter configurations cannot meet these needs, while lack of understanding and validated tools on advanced high speed configurations (compounds, coaxial rotors, lift-offset rotors, and advanced technology tiltrotors) necessitates continued research on high speed, slowed rotors.

A lack of high quality, well instrumented experimental data has limited the research progress for high advance ratio configurations. There have been only four large-scale experimental investigations to understand the performance characteristics of rotors operating at high advance ratios: the Pitcairn PCA-2 Autogiro rotor [2], a two-bladed teetering rotor [3] in the NACA Langley 30- by 60-Foot wind tunnel, the H-34 articulated rotor with zero twist blades [4], and a reduced diameter UH-1D teetering rotor [5] in the NASA Ames 40- by 80-Foot wind tunnel. Because these test data have been limited to rotor performance and blade motions, further understanding and systematic correlation efforts have been difficult. Using the previous datasets, modern analyses such as comprehensive codes have been applied and compared against theoretical analysis and data by Harris [6], Floros and Johnson [7], Quackenbush [8], Yeo and Johnson [9], and Ormiston [10]. However, lack of detailed experimental properties and data hinder evaluation of the higher fidelity methods.

The earliest high-fidelity computational fluid dynamics (CFD) predictions of high advance ratio flows were made by Strawn in 2003 and Theron in 2006. These unpublished works were later examined and documented by Harris [6]. Both calculations were fundamental efforts to establish a baseline for CFD accuracy using idealized test cases. de Montaudouin [11] examined an autogyro and provided a visual understanding of the wake roll-up using CFD. All three CFD studies used the overset, structured mesh OVERFLOW 2 flow solver.

The recent full-scale UH-60A slowed rotor test in the US Air Force National Full-Scale Aerodynamics Complex [12] bridges the gap in datasets and provides an opportunity to gain a more thorough insight into high advance ratio flight. This extensive and high quality database provides a unique and comprehensive set of measurements for research and validation efforts. Recently, several researchers at the US Army (AFDD) and NASA have made use of this data for code validation and fundamental physical understanding.

Potsdam [13] performed high-fidelity CFD/CSD coupled results using Helios/RCAS software to investigate the unique aerodynamics of the high advance ratio flight regime. The research investigated airloads, surface pressures, wake visualizations, and reversed flow physics. Fundamental understanding was gained of the physics of the reversed flow region, wake interactions, advancing and retreating blade moment impulses, differential span loading, and blade deformations – as influenced by RPM and advance ratio. Performance and trim controls from CFD were also documented.

Yeo [14] applied comprehensive analysis (CA) (CAMRAD II) in order to understand the physics and quantify the comprehensive code's accuracy and reliability in the prediction of rotor performance, airloads, and structural loads at high advance ratios. Detailed comparisons were made on rotor thrust, power, propulsive force, control angles, and section loads to illustrate and understand unique aeromechanics phenomena. Kottapalli [15] also used this dataset to compare predicted performance and peak-to-peak structural loads using CAMRAD II.

Ormiston [16] discussed edgewise rotors (H-34, UH-1D, UH-60A) in terms of the fundamental aerodynamic phenomena that become important at high advance ratios. Among the investigations and comparisons performed were simplified analytical models and comprehensive analysis (RCAS) on the UH-60A configuration for performance prediction. Specifically, lift and collective control response reversal, induced power characteristics, trim issues, and profile power modeling were included.

The objective of the current work is to collect and consistently compare the results from three of these works [13,14,16] and, in the process, evaluate the strengths and weaknesses of the analytical approaches by validating against the UH-60A database. Additionally, this research is intended to complement the fundamental understanding of the high advance ratio flight gained to date.

This paper will briefly describe the UH-60A configuration and NFAC slowed rotor test. The two comprehensive analyses (software and modeling parameters) along with the CFD/CSD methodologies and models will be discussed next. Rotor performance comparisons will then be made between the experimental test data and the three analyses for advance ratios from 0.4 to 1.0, across the collective range. Airloads and structural loads will be examined for an advance ratio sweep at constant C_T/σ. Finally the effects of the RPM reduction will be investigated between experiment and CFD. The ability of the analyses to predict the magnitude and trends will be documented.

Figure 1 UH-60A rotor system installed on the Large Rotor Test Apparatus (LRTA) in the NFAC 40- by 80-Foot Wind Tunnel

UH-60A SLOWED ROTOR TEST

A full-scale UH-60A rotor (26.83 ft radius, 4-bladed, fully articulated) was tested at the U. S. Air Force National Full-Scale Aerodynamics Complex (NFAC) 40- by 80-ft wind tunnel at slowed rotational speeds - 65% and 40% of nominal – with resulting advance ratios reaching up to 1.0 [12], as shown in Fig. 1. A comprehensive set of measurements including performance, blade loads, hub loads, surface pressures, airloads, structural deformations, and PIV wake images make this data set unique. The test was part of a broader UH-60A airloads wind tunnel test program [17,18], in which the final phase of testing was the high advance ratio Slowed Rotor Test (SRT). The objective was to explore the aeromechanics of a conventional (edgewise) rotor in a non-conventional (high advance ratio) regime in anticipation of the next generation of high speed, high efficiency, variable RPM rotors. It should be emphasized that the UH-60A rotor was not designed to operate at high advance ratio, and in many respects is not optimal for this flight regime, due to its high, non-linear twist (-16 deg), for example. It also has a non-aerodynamic shank and doubler region (Fig. 2) which is not suitable for high speed flight. Some of the high advance ratio phenomena identified in this unique test are more interesting for tool validation and development (CFD, CSD, CA, analytical) and fundamental understanding than for application to realistic high-speed rotorcraft design.

The SRT test was constructed as a parametric sweep with a tip Mach number settings of 0.65 at 100% nominal RPM (258 RPM), 0.42 at 65% RPM, and 0.26 at 40%

RPM. There were a total of 232 points acquired at 3 RPMs and 3 shaft angles. At each test point, the rotor was manually trimmed to minimize 1/rev root flapping. By the SRT phase, many blade pressure transducers had become inoperable. Therefore, integrated airloads are available only at 3 stations (22.5, 86.5, 92.0% span). The rotor shaft angle was corrected to include wind tunnel wall effects.

COMPUTATIONAL METHODOLOGIES AND MODELING

Helios

The HELIcopter Overset Simulations software (Helios) is a multi-disciplinary computational platform being developed by the DoD High Performance Computing Modernization Office (HPCMO) Computational Research and Engineering Acquisition Tools and Environments Program (CREATE – Air Vehicles) and the US Army. It includes modular software components for near-field and far-field computational fluid dynamics (CFD), off-body adaption, domain connectivity, rotorcraft comprehensive analysis and computational structural dynamics (CSD), mesh motion and deformation, and a fluid-structure interface [19]. The basis of the Helios aerodynamics solution procedure is a dual-mesh paradigm that consists of unstructured meshes in the near-body region, for ease of grid generation, and Cartesian meshes in the off-body region, for accuracy and efficiency.

The near-body CFD solver in Helios is NSU3D, which is an unsteady Reynolds-Averaged Navier-Stokes (URANS) code for unstructured meshes. It utilizes a node-centered scheme that is 2nd-order accurate in space and time. A backward Euler formulation along with a dual time-stepping scheme is employed for iterative convergence at each physical time step. The Spalart-Allmaras turbulence model is used. The Cartesian off-body solver in Helios (SAMARC) is a combination of the block structured meshing infrastructure SAMRAI and the ARC3DC solver. The off-body CFD solver uses a temporally 3rd-order explicit Runge-Kutta time integration scheme and a 5th-order central difference spatial scheme with scalar artificial dissipation. The fully automated domain connectivity formulation is provided by the Parallel Unsteady Domain Information Transfer (PUNDIT) component. The Rotorcraft Comprehensive Analysis System (RCAS) is used within Helios for CFD/CSD coupled analyses. The procedure is the standard loose (delta) coupling.

An unstructured mesh has been generated for the UH-60A configuration. Each unstructured blade mesh has 3.9 million nodes, with 61,000 points on the surface. The mesh includes clustering in the volume grid around the blade tip to help resolve the tip vortex. For the off-body Cartesian grids, the finest level has a spacing of 5% chord in the wake. A uniformly refined box surrounds the rotor. The complete mesh has 15.4M near-body nodes (36.5M cells) and 145 million active off-body points. A 0.1 deg azimuthal time step is used. The meshes and flow solver setup are further detailed in Refs. 13 and 19.

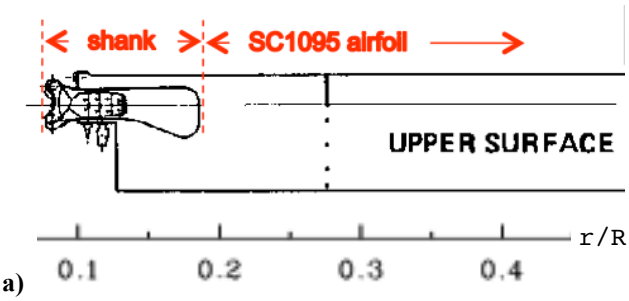

a)

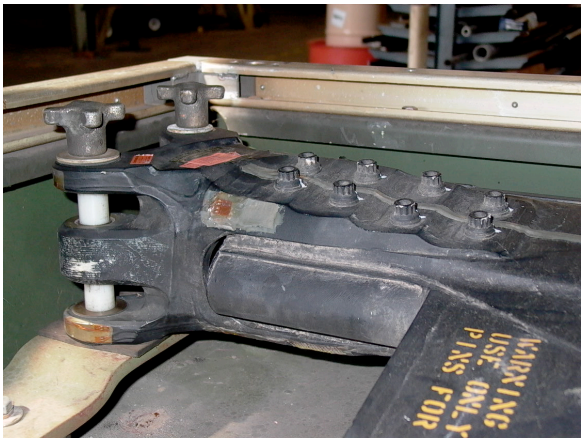
b)

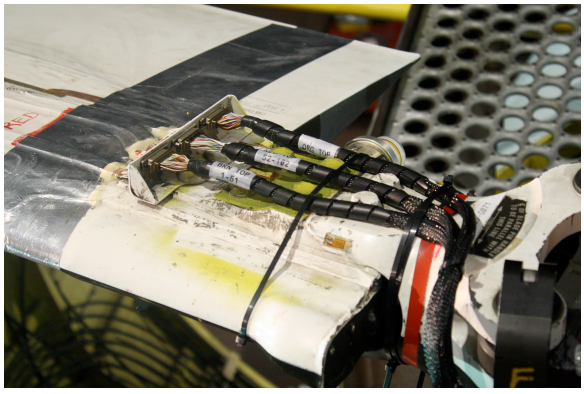
c)

Figure 2 UH-60A blade: a) planform, b) clean shank, c) instrumented shank

RCAS

The Rotorcraft Comprehensive Analysis System (RCAS) [20] is an advanced computational analysis system for rotorcraft. It is a comprehensive, multi-disciplinary system capable of modeling a complete range of complex rotorcraft configurations operating in hover, forward flight, and maneuvering flight conditions. RCAS is designed to perform a wide variety of rotorcraft engineering analyses including vehicle performance, aerodynamics and rotor loads, vehicle vibration, flight control analyses, aeroelastic stability, flight dynamics, and flight simulation. The RCAS structural model employs a hierarchical, finite element, multi-body dynamics approach for coupled rotor-body systems with multi-load path structures.

An RCAS model of the UH-60A represents the elastic blades and control system kinematics with 13

nonlinear beam elements along with rigid bars, springs, dampers, and hinge elements. The airloads modeling includes airfoil tables, linear unsteady airloads, no yawed flow, and no radial drag. The wake inflow is represented with a 91-state, 12x12 Peters-He dynamic inflow model. Results with the prescribed vortex wake are in close agreement with dynamic inflow but have more convergence issues, so it is more practical to use dynamic inflow for the extensive performance results. Airloads and structural loads are calculated using the prescribed wake with modeling parameters similar to the CAMRAD II prescribed wake analysis. The baseline RCAS model, with only minor differences, is also used for the CFD/CSD coupling in Helios.

CAMRAD

CAMRAD II is an aeromechanics analysis of rotorcraft that incorporates a combination of advanced technologies, including multi-body dynamics, nonlinear finite elements, and rotorcraft aerodynamics [21]. CAMRAD II has been used extensively for correlation of performance and loads measurements of the UH-60A in various flight conditions [22,23] and performance of the full-scale H-34 rotor and UH-1D rotor at high advance ratios [9]. The aerodynamic model is based on second-order lifting line theory. This problem is modeled within CAMRAD II as two-dimensional, steady, compressible, viscous flow (airfoil tables), plus corrections for swept and yawed flow, span-wise drag, unsteady loads, and dynamic stall. The wake model of lifting line theory is an incompressible vortex wake behind the lifting line with distorted geometry and rollup.

In this work, an isolated rotor is modeled as a flexible blade with nonlinear finite elements. Detailed rotor control system geometry and stiffness and lag damper are also incorporated. A dual-peak rigid vortex wake model is used, which makes the assumption that there may be two bound circulation peaks (inboard and outboard peaks of opposite sign). Reverse and yawed flows are important for the rotor performance correlation at high advance ratio and the current analysis includes both. Yawed flow over the blade section is accounted for using effective dynamic pressure and angle-of-attack of the yawed section and an estimate of the radial drag. Details of the modeling are given in Ref. 14.

Trim

All calculations use a cyclic trim condition of zero 1/rev flapping angle at the blade root flapping hinge. In the comprehensive analyses, calculations are run using the experimental collective values for all advance ratios. In CFD the thrust trim condition for low advance ratio, less than 0.8, is the experimental thrust. At higher advance ratios, it was not always possible to obtain the measured thrust due to the shallow thrust vs. collective curve. In these cases the collective has been fixed at the experimental value. The shaft angle is as prescribed from the corrected test value.

RESULTS

The data points which have been examined in this effort are indicated in Fig. 3 and outlined in Table 1. Almost all calculations are made at 40% rotor RPM. The performance calculations have been performed at zero shaft angle with collective sweeps at μ = 0.4, 0.6, 0.8, 0.9, and 1.0 (◇). An advance ratio sweep (μ = 0.4, 0.5, 0.7, 0.9) at $C_T/\sigma \approx 0.063$ investigating airloads and structural loads was run at a 4 deg shaft angle (□). A comparison of structural loads is also performed between the baseline (100% RPM) and slowed rotors.

In the following sections, discussion will first focus on the overall performance predictions, including the effect of shank modeling. Subsequent sections investigate the airloads and structural loads comparisons, documenting the current capabilities of state-of-the-art analyses for high advance ratio conditions.

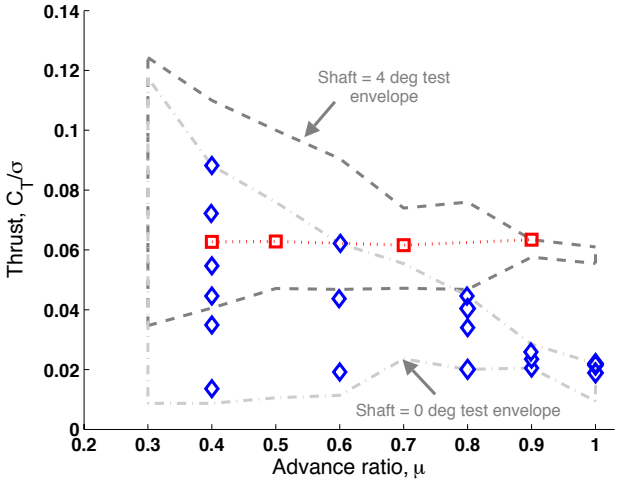

Figure 3 Wind tunnel test envelope and analysis points

Rotor Performance

Rotor performance includes the prediction of not only thrust, torque and drag, but also the collective and cyclic control inputs required to obtain a trimmed result. The issues related to the UH-60A shank modeling in comprehensive analysis and CFD as well as the associated correlation/computation of the shank section drag are discussed first.

Shank Modeling

Previous studies showed that inclusion of shank and doubler drag for the performance calculation of the H-34 and UH-1D rotors at high advance ratio made a significant improvement in correlation [6,9,14,16]. A similar approach was taken for the current analyses. The planform of the UH-60A blade shank is illustrated in Fig. 2a. The initiation of the SC1095 airfoil section is around 19% span. Inboard of this point the airfoil thickens and becomes non-aerodynamic. The root cutout is at

r/R = 0.13. A short section between the root end grip (r/R = 0.09) and cutout (r/R = 0.13) generates considerable drag (Fig. 2b). Wiring for pressure transducers and strain gauges on two of the blades, shown in Fig. 2c, generates additional drag. No calculations conducted so far for the UH-60A in a conventional flight regime included realistic root end geometry. It should be noted that interference effects of the hub, except for the standard hub tare methodology, have not been quantified and may also be a source of drag data inaccuracy.

For this effort, both comprehensive analyses, RCAS and CAMRAD, include an airfoil table for the shank region with a significantly increased drag. In the RCAS results, the blade shank drag coefficient is taken to be 1.5, and this high value partly compensates for not including contributions of yawed flow and radial drag. Otherwise, it is probably unrealistically large. The CAMRAD analysis model includes the inboard blade shank (r/R < 0.13) with a constant drag coefficient of 0.4 and a shortened chord of 0.69 ft and the non-aerodynamic full-chord section (0.13 < r/R < 0.19) with a constant drag coefficient of 0.01. It should be noted that the comprehensive analysis shank drag values were estimated based on obtaining good correlation with measurements, as no independent data on drag of the shank was available at the time. CAMRAD was correlated to best match experimental induced plus profile power, while RCAS was correlated to both torque and drag independently.

The CFD calculations use a first principles-based approach which is not based on correlation with data. The shank region was measured, geometrically approximated, and gridded using an unstructured mesh as shown in Fig. 4b. Previously, a faired root region (Fig. 4a) had been used in calculations [13,19]. From the CFD calculations an estimate of the shank drag on the shortened chord grip and spar section (r/R = 0.09–0.13, see Fig. 2a) can be obtained for comparison with the comprehensive code values. Figure 5 shows the x-force coefficients (M^2c_x and c_x) as a function of azimuth for a $\mu = 1.0$ case with a 0 deg collective and rigid blades. The x-force is in the in-plane "chord-wise" direction in the rotating hub coordinate system. X-force coefficient, c_x, is non-dimensionalized by the local velocity. Spikes in c_x, as the airfoil section enters/leaves the reversed flow region and the local velocity goes to zero, have been removed. Positive x-force is towards the trailing edge. M^2c_x represents a dimensional in-plane force on the section and allows a comparison of the relative force contributions of each section. The grip and shank inboard-most section (centered at r/R = 0.11) has an average x-force coefficient (c_x) of 0.14 and 0.18 on the advancing and retreating sides, respectively. This can be approximated as the drag and then compared with the values used in the comprehensive analyses (i.e. CAMRAD shank $c_d = 0.4$). As a double check, the section at r/R = 0.775, which is at zero pitch, shows advancing and retreating CFD x-force coefficients of 0.0092 and 0.024, respectively, which are close to the airfoil table zero angle of attack drag values of 0.0085 and 0.02. Note that even at zero collective (at 0.75R) the root section has 9.5 deg of built-in twist.

Table 1 Analysis test data points

Point^	M_{tip}	μ	C_T/σ	α_s	θ_0 *	θ_{1c}	θ_{1s}
baseline (100% RPM)							
6912	0.65	0.4	0.0712	0	6.0	-1.1	-4.8
$\mu = 0.4$ collective sweep							
9122s	0.26	0.4	0.0136	0	0.0	-0.7	-1.4
9123	0.26	0.4	0.0349	0	1.9	-0.1	-3.0
9121	0.26	0.4	0.0446	0	3.0	0.5	-3.8
9124	0.26	0.4	0.0547	0	3.9	0.7	-4.7
9125s	0.26	0.4	0.0722	0	6.0	1.7	-6.5
9126	0.26	0.4	0.0882	0	8.0	2.6	-8.4
$\mu = 0.6$ collective sweep							
9141s	0.26	0.6	0.0192	0	0.0	-1.6	-1.0
9143	0.26	0.6	0.0325	0	3.9	-1.2	-3.1
9145	0.26	0.6	0.0437	0	7.9	-1.0	-5.4
$\mu = 0.8$ collective sweep							
9155s	0.26	0.8	0.0201	0	**2.0**	-2.8	-3.0
9157	0.26	0.8	0.0340	0	**4.0**	-2.9	-5.9
9158	0.26	0.8	0.0404	0	**6.0**	-2.9	-8.3
9159s	0.26	0.8	0.0446	0	**8.0**	-2.6	-10.8
$\mu = 0.9$ collective sweep							
9162s	0.26	0.9	0.0205	0	**0.0**	-3.7	-0.3
9163	0.26	0.9	0.0235	0	**2.0**	-4.0	-3.0
9164	0.26	0.9	0.0259	0	**4.0**	-4.4	-6.0
$\mu = 1.0$ collective sweep							
9169s	0.26	1.0	0.0215	0	**-0.1**	-4.8	0.0
9167	0.26	1.0	0.0189	0	**0.9**	-4.8	-1.4
9175s	0.26	1.0	0.0220	0	**1.9**	-5.1	-2.7
advance ratio sweep at constant C_T/σ							
9318s	0.26	0.4	0.0627	4	2.0	0.7	-4.0
9325s	0.26	0.5	0.0628	4	2.0	0.1	-4.8
9518s	0.26	0.7	0.0616	4	3.0	-0.8	-6.9
9528s	0.26	0.9	0.0634	4	6.2	-3.1	-11.6

* CFD/CSD fixed collective trim cases in **bold**
^ CFD/CSD test points with shank geometry indicated by s

The grip/shank section generates no lift, while the non-aerodynamic full-chord section (centered at r/R = 0.15) generates approximately 50-80% of the lift coefficient compared to the neighboring clean section (r/R = 0.225). A drag force on the non-aerodynamic full-chord lifting section was not able to be obtained because it is difficult to determine the section angle of attack from CFD.

CFD calculations for the performance prediction test points (Table 1) were originally performed using the faired root end (Fig. 4a) [13]. It was not feasible to rerun all these cases with the approximated shank geometry. Instead only the lowest (zero) and some of the highest collective test points were rerun, as indicated in the table. Drag and torque increments between the faired and shank calculations at zero collective were then computed and added to the faired root performance results in order to obtain a full collective sweep for the shank geometry. It will be seen that adding the zero collective shank increment is a good approximation since only a small collective dependency was noted. The high collective points with the shank will be shown in the plots. Trim controls did not change to any degree based on the root end treatment.

Performance Parameters

The cyclic controls predicted by CAMRAD and Helios for the range of advance ratios are compared with test data in Figs. 6 and 7. The experimental fixed system control measurements have an accuracy of 0.1-0.3 deg [17]. The lateral cyclic, θ_{1c}, (Fig. 6) is well predicted, except at high thrust and low advance ratio. At $\mu = 1.0$, it is seen that there is very little sensitivity to lateral cyclic. The CFD angles are about 1 deg more negative, and this may be the result of a thrust discrepancy. CAMRAD is in better agreement at the highest advance ratio, although the predictions at $\mu = 0.9$ are somewhat poorer. Figure 7 shows that the longitudinal cyclic, θ_{1s}, is very well predicted at the lowest advance ratio. At higher advance ratios the slopes are in good agreement but the absolute values are offset, but typically by less than 1 deg. CFD results saw no change in cyclic control with the addition of the shank geometry.

Thrust vs. collective for all three analyses is shown in Fig. 8. The agreement between the analyses is quite good, the largest outlier being the Helios results at $\mu = 0.8$. The zero collective RCAS results appear to cluster lower than the CAMRAD and Helios results by about $C_T/\sigma = 0.005$.

Compared with the data all thrust vs. collective analyses show good agreement in slope across the advance ratios. The overall thrust levels are reasonably well predicted. However, the experimental trends, especially at $\mu = 0.8$, warrant further investigation as the data at zero collective appears to be out of line with the linear behavior at higher collectives. A weak thrust reversal trend at $\mu = 1.0$, where increasing collective reduces the rotor thrust, is captured by Helios and CAMRAD. The thrust reversal in the test data is denoted by a single data point at 1 deg collective. RCAS does not predict this phenomenon.

In Fig. 8 as well as subsequent figures, the CFD results for the configuration with shank geometry at the highest collectives are shown as discrete filled symbols (see Table 1). As explained previously, the CFD curves have been shifted based on the zero collective increment. The high collective points indicate the extent to which the shank effects are a function of collective. When the high collective points lie on the CFD lines there is no collective dependence, while any disagreement between the trend lines and the high collective shank results indicate that the zero collective increment is not uniform across the collective range.

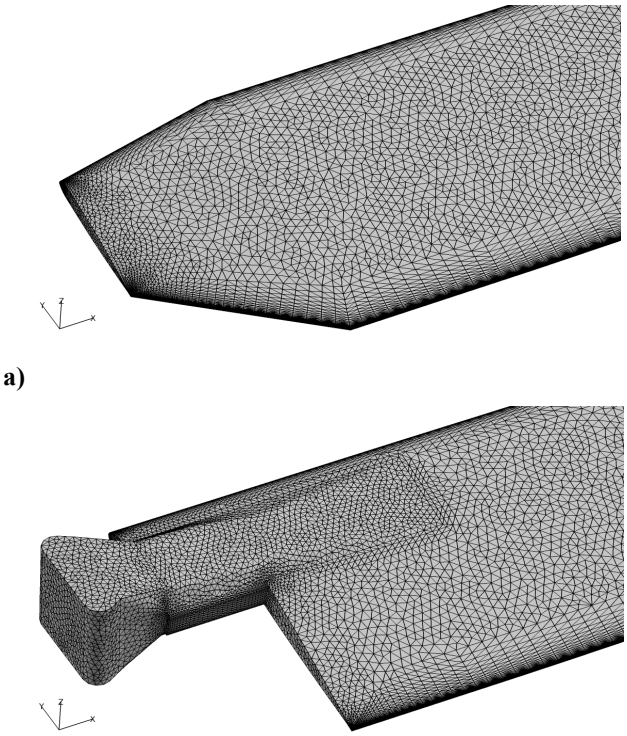

a)

b)

Figure 4 CFD root geometry: a) baseline, b) shank approximation

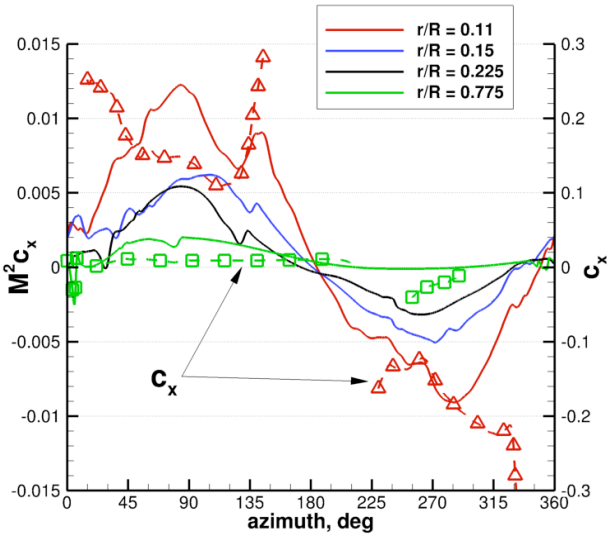

Figure 5 UH-60A shank x-force coefficient, $\mu = 1.0$, $\theta_0 = 0$ deg, rigid blades: —— M^2c_x, – □ △ – c_x

For the low advance ratios it was possible to trim to thrust in CFD, and the collective angles are in agreement with test to less than 1 deg. At higher advance ratios, it was not possible to trim to thrust due to the lack of thrust sensitivity to collective control input, e.g. in the $\mu = 1.0$ case all collective angles give essentially the same thrust. These fixed collective runs show more significant differences. What is essentially a thrust offset discrepancy could be attributed to hub interference, erroneous lift predictions in the reversed flow region, and/or experimental issues.

Figure 9 shows the drag predictions and comparison with the data. The overall drag levels are relatively consistent between the analyses, but markedly different from experiment, especially at higher advance ratio, where results are off by 10-15%. Only at $\mu = 0.4$ are the drag levels in agreement between test and analysis. The slope of the CFD curves are in noticeably better agreement with the data, while both comprehensive analyses tend to under-predict the slopes. The CFD shows minimal shank drag dependence with collective.

Figure 10 shows the torque comparisons as a function of collective for the various advance ratios. All analyses significantly over-predict the torque magnitude, by upwards of 100%. RCAS results appear in better agreement, but still over-predict. The trend agreement among analyses is poor. At the higher advance ratios the CFD trends are best (e.g. $\mu = 0.8$), while at the lower advance ratios perhaps the comprehensive analyses hold an edge.

Figure 11 plots the combined torque and drag power from Figs. 9 and 10 (i.e. $C_Q + \mu C_D$) as the rotor "total" power, C_{Ptot}, recently defined by Ormiston [24]. This is a more direct way of presenting the combined power components than the alternative equivalent nomenclature of profile plus induced power ($C_{Po} + C_{Pi}$) that is often used. The reasonable agreement here is fortuitous given that all the analyses overpredicted the torque and underpredicted the drag. The CFD curves appear to capture the experimental data trends. The CAMRAD magnitudes are best, but recall that the shank drag coefficient was chosen in order to match this parameter. Thus the CAMRAD analysis matches at zero collective but is not in agreement at higher collectives due to a slope discrepancy that cannot be captured.

Figures 12, 13, and 14 compare the drag, torque, and total power as a function of advance ratio for 0 deg collective. In Fig. 12 the drag trend shows strong dependence on advance ratio due to the non-standard normalization based on tip speed, and also the rotational effects of advancing/retreating side velocity differences. The three analyses are in good agreement but all under-predict the data. The effect of the shank increment is shown for RCAS and Helios. The RCAS increment is rather large, probably due to the large c_d assumption. The Helios increment due to the shank is much smaller, and is negligible at $\mu = 0.3$, as would be expected.

Torque prediction is shown in Fig. 13. In general the agreement is poor. The overall level of the RCAS results

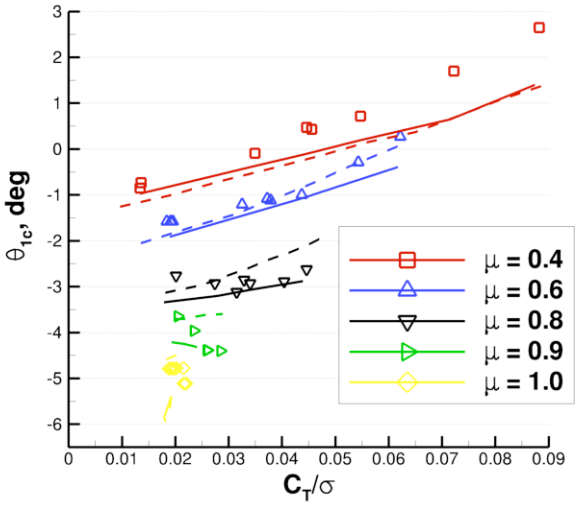

Figure 6 Lateral cyclic vs. thrust: symbols – test, —— Helios, – – – CAMRAD

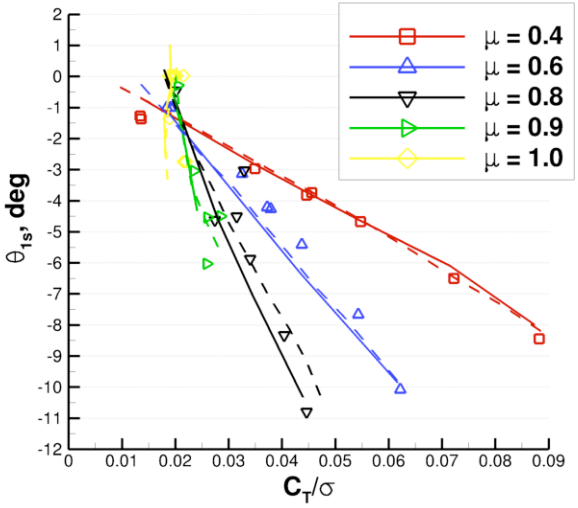

Figure 7 Longitudinal cyclic vs. thrust: symbols – test, —— Helios, – – – CAMRAD

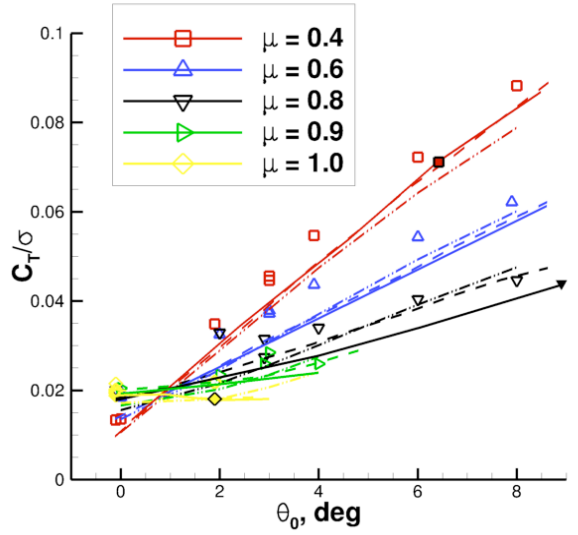

Figure 8 Thrust coefficient vs. collective: symbols – test, —— Helios, – – – CAMRAD, –··– RCAS

is somewhat correct but the trend is wrong. Similarly, the CAMRAD result is off in both magnitude and trend. CFD correctly captures the decreasing torque trend at higher advance ratio, but the magnitude is significantly (up to 50%) overpredicted. The reduction in torque with increasing advance ratio is a trend towards autorotation that apparently cannot be well captured by the comprehensive analyses. Conclusions regarding the total power shown in Fig. 14 are similar to those made for Fig. 11, and the plot is shown for completeness. It should be noted that at the higher advance ratios, the torque contribution to total power is relatively small (< 10%).

In summary, in comparison with the data, all analyses under-predict drag and significantly over-predict torque. This is particularly apparent at the high advance ratios, while at conventional advance ratios (0.4), all analyses are in good agreement with the data, as might be expected. This mismatch in torque and drag appears to make the total power comparison more favorable than it really is. In comparison with the data, CFD trends with collective or advance ratio appear in most cases to be more accurate, in spite of overall magnitude discrepancies.

CFD for Performance Prediction

The current results not withstanding, for many reasons performance prediction, particularly for rotorcraft, is not a strong suit for CFD: 1) For helicopter design a large number of flight conditions are required, and CFD is currently too expensive for such a large matrix of test cases. While the CFD/CSD performance and loads presented herein are generally seen to be an improvement over the comprehensive analyses, the calculations were several orders of magnitude more expensive. 2) Comprehensive analysis has shown excellent ability to correlate with global performance measures from wind tunnel and flight test data [23], in spite of not always correctly capturing the detailed flow physics and the need, as shown here, to use empirical corrections. 3) Even for fixed wing configurations, CFD drag prediction is a difficult and unsolved problem, as evidenced by the ongoing work of the AIAA Drag Prediction workshop [25]. The unsteady, vortical nature of rotorcraft flow fields make drag and torque prediction especially difficult, although researchers have make significant progress in wake prediction with advancements such as higher-order schemes and adaptive mesh refinement [e.g. 19]. 4) Performance prediction can be highly dependent on numerical modeling parameters, grid density, and, for more severe flight conditions, turbulence modeling. Although no grid sensitivity studies were performed for the current CFD calculations, Ref. 13 showed that two different CFD/CSD analyses – Helios/RCAS and OVERFLOW/CAMRAD II – are in good agreement with each other at $\mu = 1.0$, indicating no systemic numerical issues with the current CFD analyses, but not necessarily grid convergence. Nonetheless, it is important to benchmark the current state-of-the-art CFD capabilities against test and other state-of-the-art comprehensive and engineering analysis methods.

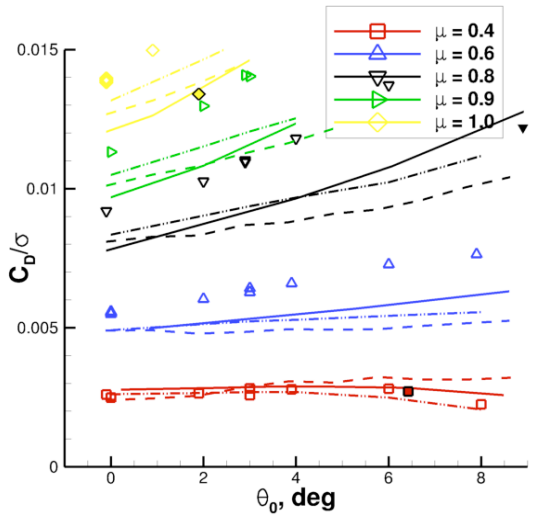

Figure 9 Rotor drag coefficient vs. collective: symbols – test, —— Helios, – – – CAMRAD, –··– RCAS

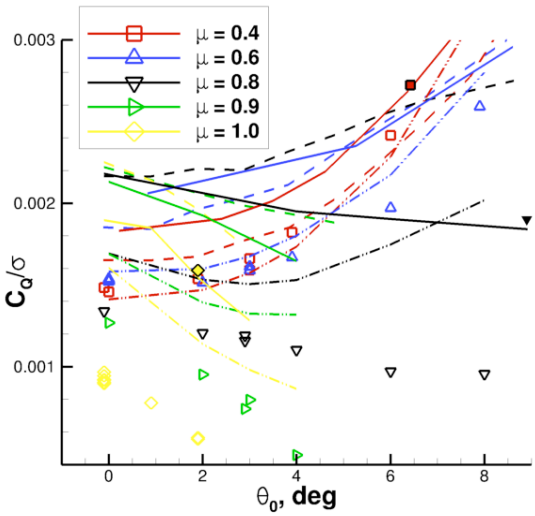

Figure 10 Rotor torque coefficient vs. collective: symbols – test, —— Helios, – – – CAMRAD, –··– RCAS

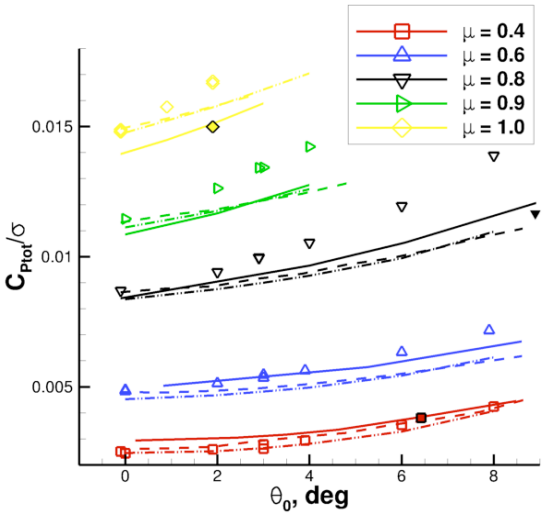

Figure 11 Rotor "total" (torque plus drag) power vs. collective: symbols – test, —— Helios, – – – CAMRAD, –··– RCAS

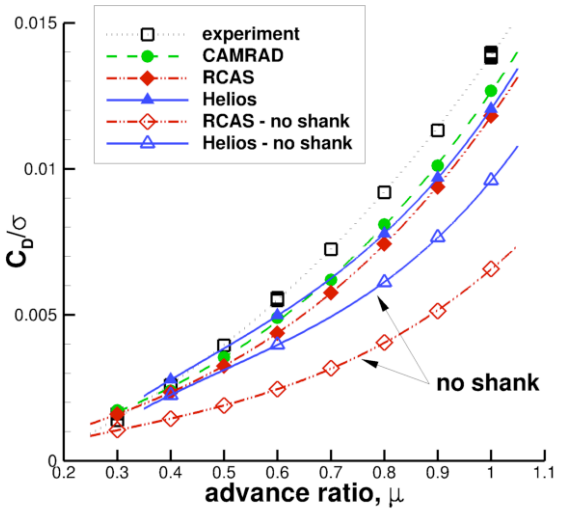

Figure 12 Rotor drag coefficient vs. advance ratio, zero collective

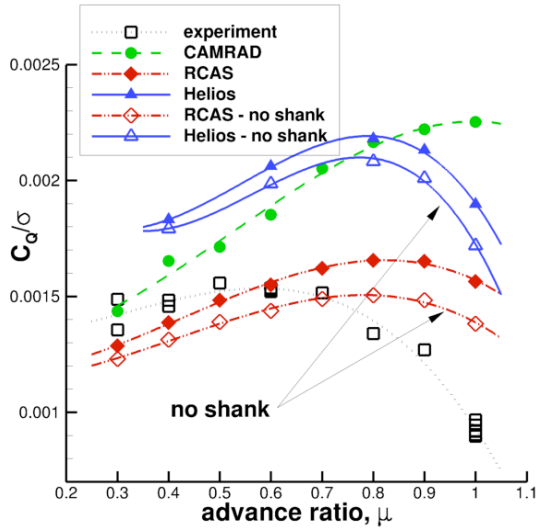

Figure 13 Rotor torque coefficient vs. advance ratio, zero collective

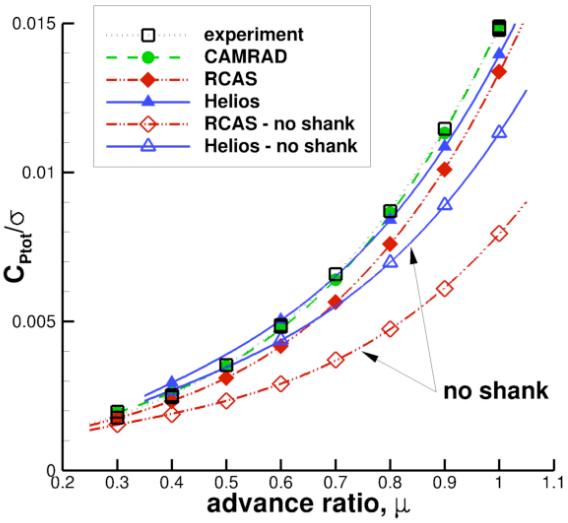

Figure 14 Rotor "total" (torque plus drag) power vs. advance ratio, zero collective

Detailed Shank Effects

While the shank has a significant effect on rotor performance at high advance ratio, the resulting flow field details are more subtle. The airloads show almost no effect due to the geometry changes, as the trim was unaffected. There are very minor airload differences around 0 deg azimuth outboard (not shown), presumably due to different vortices trailing from the root end in the hub region. The flow field differences are shown in Fig. 15. The faired geometry appears to create a strong root vortex at 90 deg azimuth and a leading edge vortex at 180 deg azimuth, which the shank geometry does not. In spite of these differences, the addition of the hub and LRTA fuselage is required for truly realistic simulations in this region.

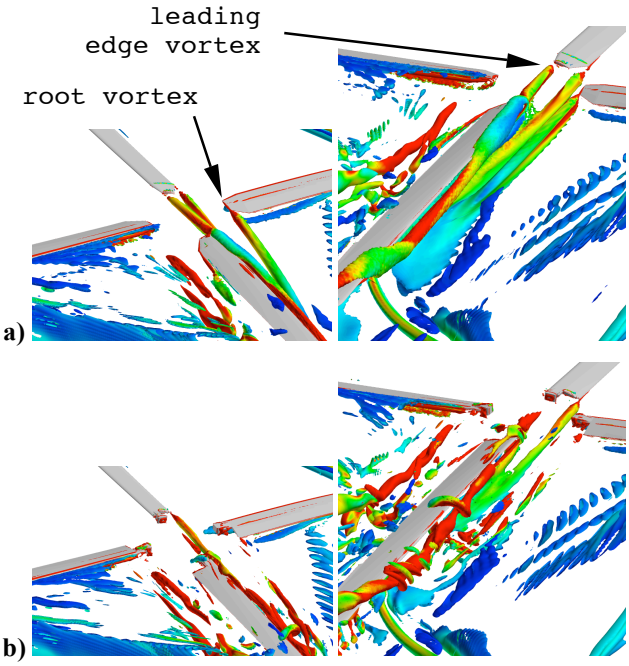

Figure 15 Root flow field differences due to shank modeling, $\mu = 1.0$, $C_T/\sigma = 0.022$ (9175): a) faired root, b) shank model

Airloads

Airloads are examined for an advance ratio sweep ($\mu = 0.4$, 0.5, 0.7, and 0.9) at a nominal 4 deg shaft angle and $C_T/\sigma = 0.063$. Details of the test points are shown in Table 1 under "advance ratio sweep at constant C_T/σ". These points match those investigated in Ref. 14. Figures 16 and 17 show the calculated normal force and pitching moment distributions at r/R = 0.225 and 0.92 across the advance ratio range in comparison with test data. Recall that both CAMRAD and RCAS use a prescribed vortex wake with dual-peak model. For normal force, all analyses capture the main features of the airloads and trends with advance ratio, including the advancing side negative loading and sharp drop at 0 deg azimuth outboard. At the lower advance ratios the negative

loading is underpredicted by Helios and CAMRAD, while RCAS over-predicts this loading. CAMRAD significantly under-predicts the inboard (r/R = 0.225) advancing side loading. The prescribed wake models appear to accentuate the blade-wake interactions, resulting in normal force oscillations in the 1st quadrant that are not seen in the data or CFD.

The pitching moment comparisons among the analyses are in general agreement. All analyses over-predict the reversed flow pitching moment (r/R = 0.225), except at $\mu = 0.9$. The lifting line models have difficulty as the blade enters the reversed flow region in the 3rd quadrant, generating spikes in both normal force and pitching moment. All the calculated pitching moments are also significantly more positive in the advancing side negative loading region (r/R = 0.92). This is especially curious because CFD has shown good capability to predict this phenomenon for the baseline rotor where the large negative pitching moment is a transonic effect. That is not the case here because the advancing tip Mach number at the highest advance ratio ($\mu = 0.9$) is only 0.49. This is a flow regime where both CFD and comprehensive analyses should be accurate for pitching moment prediction.

A detail of the CFD and experimental chord-wise pressure distribution at r/R = 0.92, 90 deg azimuth for $\mu = 0.9$ is shown in Fig. 18. The lower surface leading edge suction is significantly larger in the experiment and there appears to be bad data on the upper surface mid-chord, both of which lead to larger negative pitching moments. However, pitching moment integration without these pressure taps shows that these differences do not account for the fundamental advancing side discrepancy. With respect to the lower surface leading edge suction peak, there is no indication of flow separation in the CFD solution. The leading edge suction difference might be attributable for this case to a longitudinal cyclic difference of 2.0 deg (-9.6 and -11.6 from Helios and experiment, respectively), but this under-prediction of the advancing side pitching moment magnitude is apparent in most UH-60A slowed rotor test points [13], some of which have much better cyclic agreement. In addition to the cyclic discrepancy, the reduced peak pressure is perhaps an indication of reduced elastic pitch or a less negative angle of attack relative to the data. Harmonic analysis of the errant pitching moments (not shown) give no indication of poor prediction of a particular harmonic. It should also be noted that the mean pitching moment must be removed from the data for r/R = 0.225, otherwise the data magnitude is offset by as much as -0.008. Norman [18] systematically explored some of the differences between wind tunnel and flight test UH-60A airloads, including a large pitching moment offset, only to conclude that bad measurements or integration errors are not to blame, but that the cause is still unknown.

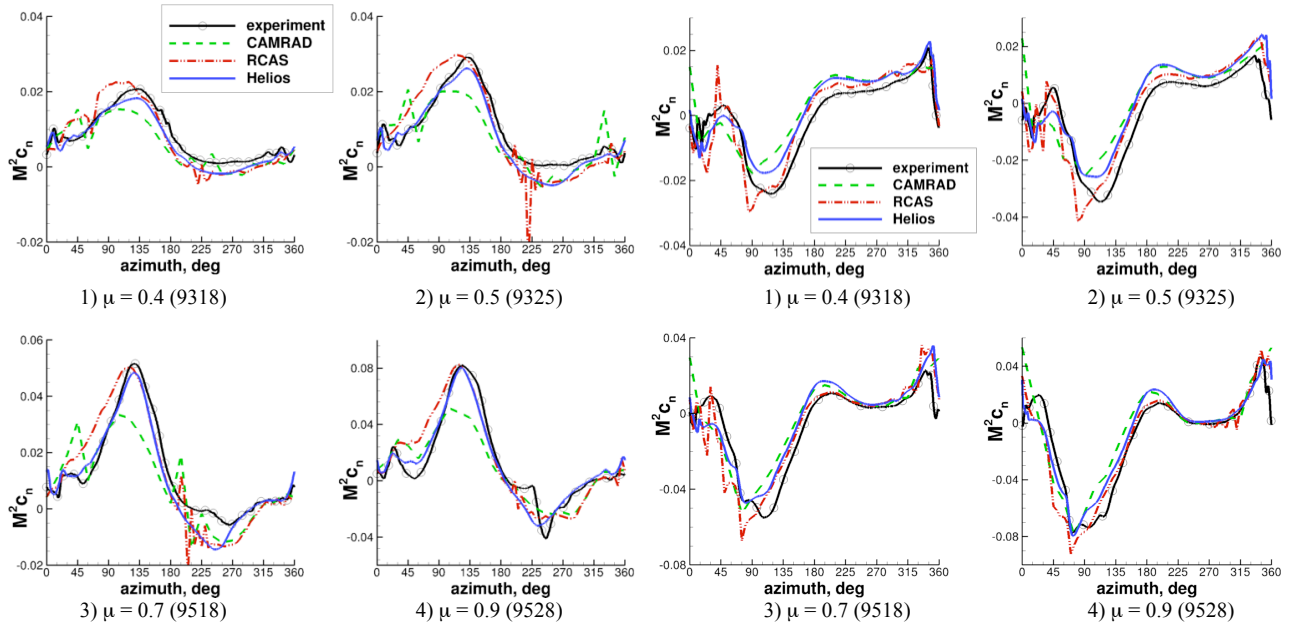

Figure 16 Normal force (M^2c_n) comparison for advance ratio sweep, $\alpha_s = 4$ deg, $C_T/\sigma = 0.063$, r/R = 0.225 and 0.92

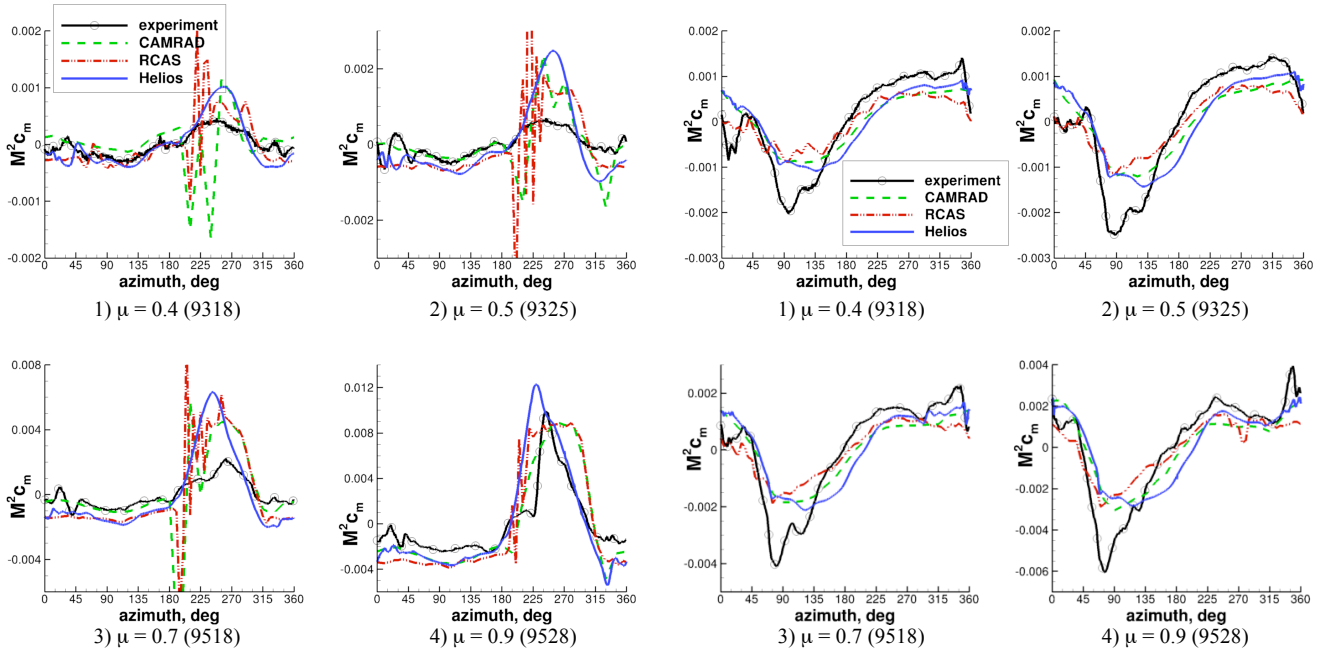

Figure 17 Pitching moment (M^2c_m) (mean removed) comparison for advance ratio sweep, α_s = 4 deg, C_T/σ = 0.063, r/R = 0.225 and 0.92

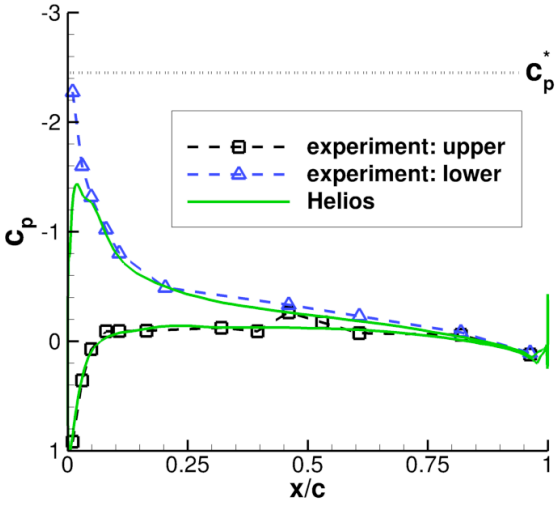

Figure 18 Chord-wise pressure distribution, r/R = 0.92, ψ = 90 deg, μ = 0.9 (9528).

Structural Loads

In this section the structural loads are compared for the advance ratio sweep at 4 deg shaft angle. Additionally, calculated CFD structural loads are compared with data between the 100% RPM nominal rotor and the 40% RPM slowed rotor.

The calculated (CAMRAD II) blade frequencies for the nominal and slowed rotors are shown in Table 2. Beyond the 2nd flap mode, the frequencies are quite different for the slowed rotor, with a significant increase in the 1st torsion frequency and no modes in the 4-6/rev range. Dominant 3/rev in the structural loads is to be expected for the slowed rotor.

Table 2 Calculated rotor blade frequencies [14]

Mode	100% RPM (/rev)	40% RPM (/rev)
lag 1	0.28	0.32
flap 1	1.04	1.05
flap 2	2.83	3.32
torsion 1	4.50	11.12
lag 2	4.69	10.54
flap 3	5.22	7.29

Advance Ratio Sweep

Figure 19a shows the oscillatory flap bending moment at 50% span for the four advance ratios. Steady values have been removed. Cross-coupling among flap bending, chord bending, and torsion moments were accounted for in the data correction process. The agreement between analyses is good, with CAMRAD mostly under-predicting the negative peak that is dominant in the 2nd quadrant. CFD peak-to-peak values are the most accurate. The increase of the peak-to-peak values with advance ratio is successfully captured. All have good waveform and phase, showing to some extent the two oscillations in the 3rd and 4th quadrants. This flap bending agreement most likely follows from the accurate normal force predictions (Fig. 16). Figure 19b shows the flap bending harmonics that contribute to vibratory loads, 3rd to 5th harmonics. As noted in the blade frequencies (Table 2), the 2nd flap mode at 3.3/rev is dominant, and the waveforms have strong 3/rev content, which is accurately captured by all the analyses. Peak-to-peak magnitudes are slightly overpredicted at the lower advance ratios and generally underpredicted at the higher advance ratios. The phase is excellent.

The oscillatory torsion moments at 50% span are shown in Fig. 20a. Here the agreement is not as consistent or clear between analyses and test. It is apparent that the low frequency waveforms are captured at all advance ratios. Figure 20b shows the vibratory components of the torsion moments. At the highest advance ratio ($\mu = 0.9$), the RCAS and Helios results are in good agreement with the test data (especially the CFD) while CAMRAD significantly overpredicts the vibratory components in addition to being slightly off in phase. At the other advance ratios the results are less satisfactory. At $\mu = 0.7$ the magnitudes are correct, but all the analyses predict different and incorrect phase. The dominant 3/rev content at low advance ratio ($\mu = 0.4$ and 0.5) is not predicted at all by any of the analyses, and the magnitudes are largely underpredicted, save perhaps the RCAS analysis. It should be noted that the vibratory magnitudes rapidly increase between $\mu = 0.7$ and 0.9, and there is approximately a factor of 5 between low (0.4) and high (0.9) advance ratio. At the lowest advance ratios, the moments are rather small (~15 ft-lbs). The overall abrupt vibratory peak-to-peak increase with advance ratio can, therefore, be predicted by the analyses. Note that the oscillatory peak-to-peak magnitudes show a steady increase with advance ratio which is also predicted. The RCAS analysis, but not the coupled Helios/RCAS result, indicates an obvious 10-12/rev harmonic content at the lowest advance ratio ($\mu = 0.4$). This is perhaps related to the blade torsion frequency in this range. However, there is no significant content in this range in the test data (harmonic analysis not shown).

The harmonic content of flap bending along the blade span is investigated in Fig. 21 for the $\mu = 0.9$ case (9528). Except for 4/rev, the analyses are mostly acceptable. CFD is particularly accurate in 2/rev and 5/rev, while RCAS faithfully captures the 3/rev. CAMRAD models the 4/rev trends but not the magnitude, and significantly under-predicts the 1 and 2/rev. Although the flap bending waveforms in the 3rd and 4th quadrants (Fig. 19a) are well predicted and appear to be comprised of 4/rev, there must be other harmonics here as well since the 4/rev harmonic analysis shows such significant differences with experimental data. The $\mu = 0.7$ case is equally underpredicted in 4/rev despite excellent waveform agreement on the retreating side (not shown).

Figure 22 shows the torsion moment harmonic analysis for the same case. While it was not obvious in the waveforms in Fig. 20a, it is clear in the harmonic breakdown that the CFD is particularly accurate for the lower harmonics. Only the inboard CFD results show any significant differences with data. RCAS and CAMRAD results are mixed. RCAS under-predicts almost all the harmonics, while the CAMRAD trends are somewhat random. Given the discrepancies in pitching moment prediction (Fig. 17), this overall level of agreement in torsion moment is perhaps surprising, and lends further impetus to continued investigation of the experimental pitching moments.

A sample edgewise bending moment result at 50% span is shown in Fig. 23 for the $\mu = 0.9$ case. Based on harmonic analysis, the lower harmonics, up to 4/rev, are captured, but the analyses contain significant high frequency content not present in the data. The correlations significantly degrade further inboard on the blade. This is known to be only partly due to improper modeling of the non-linear lag damper, which is currently modeled as linear.

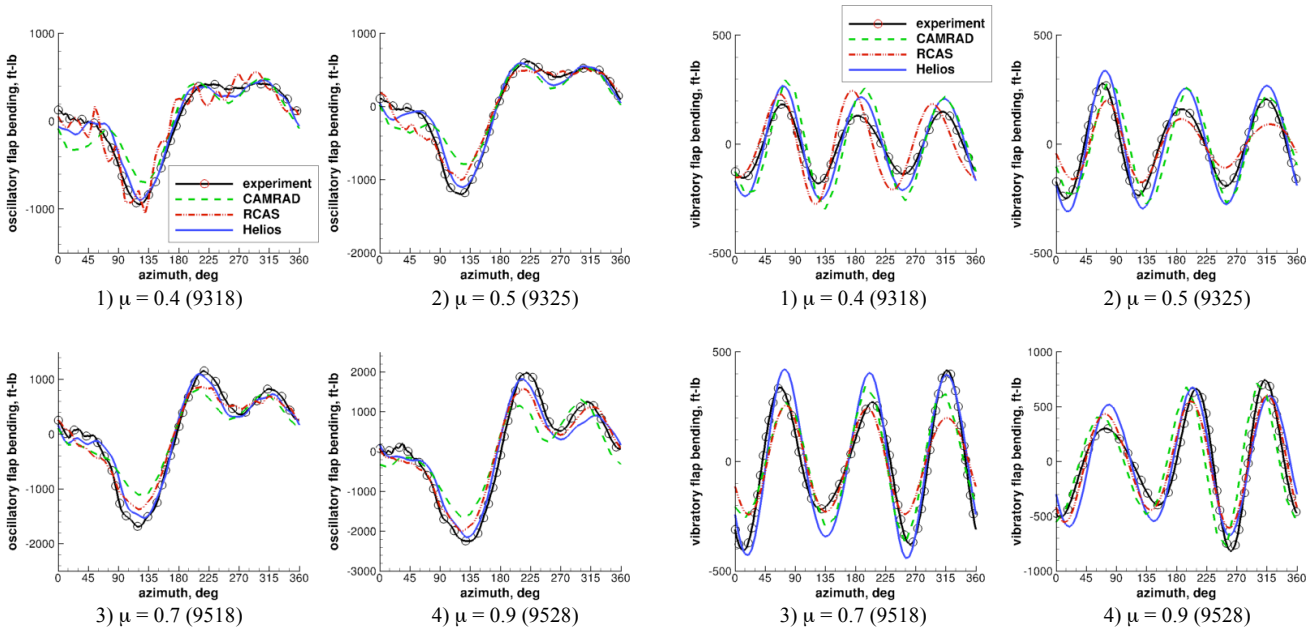

a) oscillatory flap bending **b) vibratory flap bending**

Figure 19 Blade flap bending moments for advance ratio sweep, $\alpha_s = 4$ deg, $C_T/\sigma = 0.063$, r/R = 0.50: a) oscillatory, b) 3rd to 5th vibratory harmonics

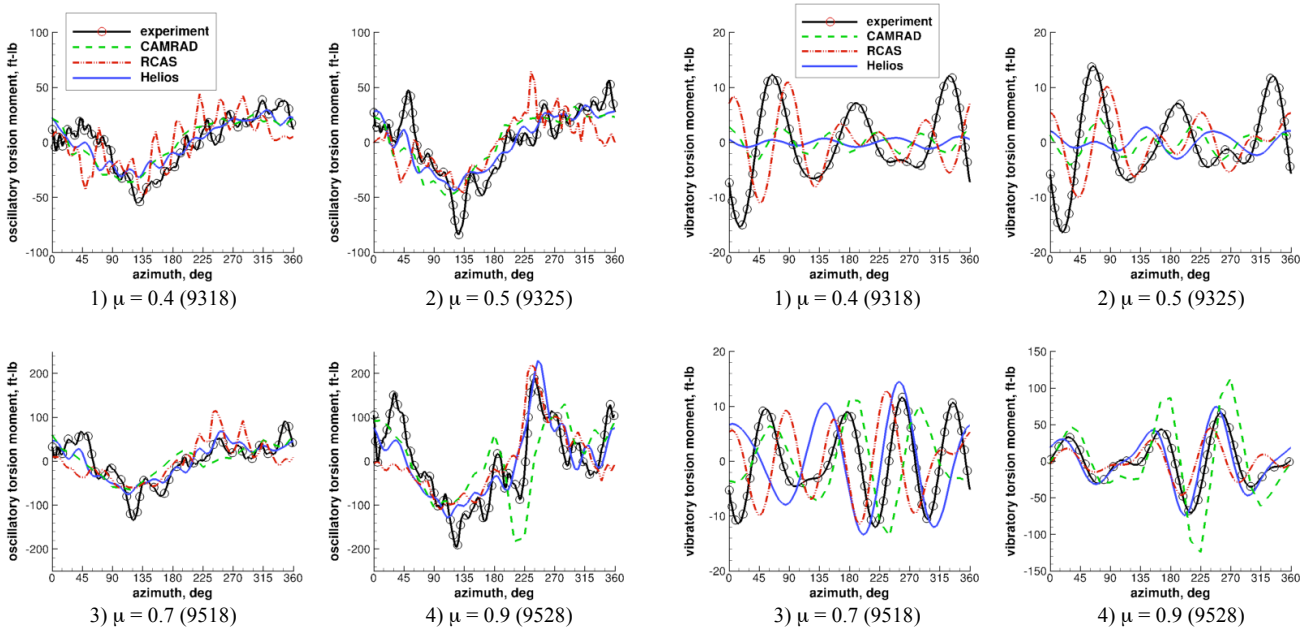

1) μ = 0.4 (9318) 2) μ = 0.5 (9325) 1) μ = 0.4 (9318) 2) μ = 0.5 (9325)

3) μ = 0.7 (9518) 4) μ = 0.9 (9528) 3) μ = 0.7 (9518) 4) μ = 0.9 (9528)

a) oscillatory torsion moment **b) vibratory torsion moment**

Figure 20 Blade torsion moments for advance ratio sweep, α_s = 4 deg, C_T/σ = 0.063, r/R = 0.50: a) oscillatory, b) 3rd to 5th vibratory harmonics

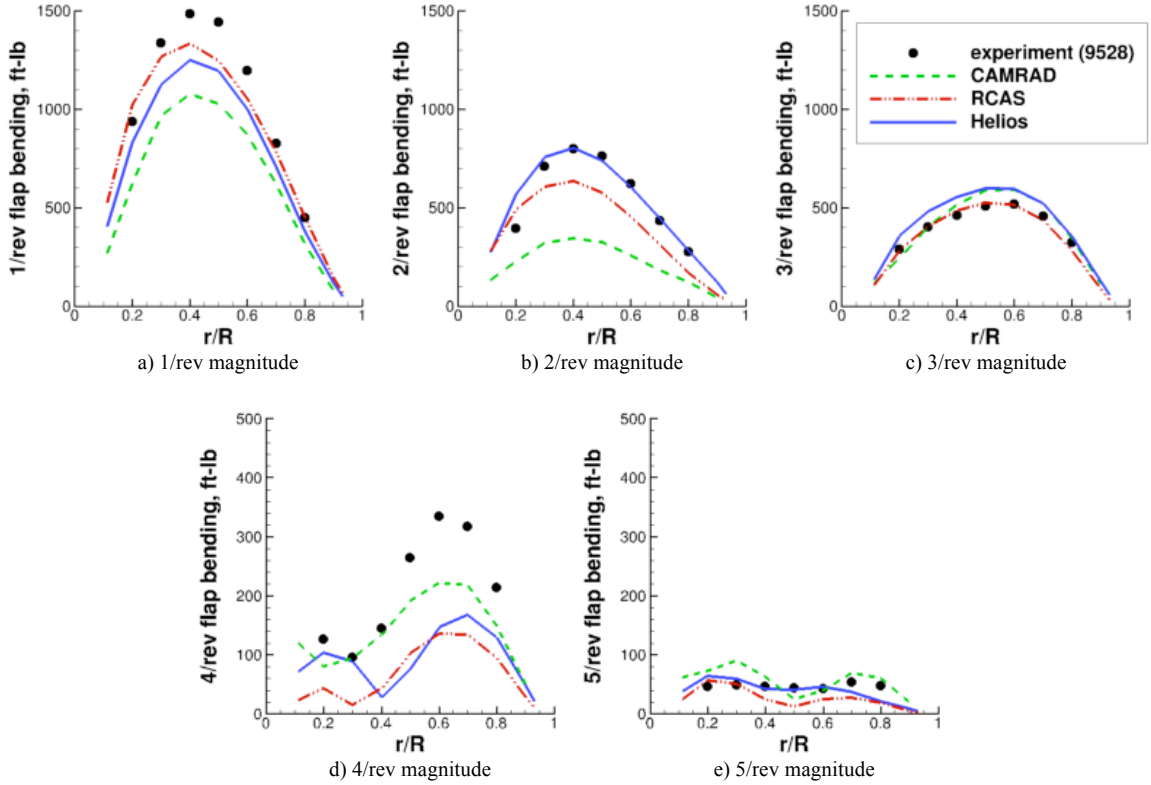

a) 1/rev magnitude b) 2/rev magnitude c) 3/rev magnitude

d) 4/rev magnitude e) 5/rev magnitude

Figure 21 Flap bending moment magnitude harmonics, μ = 0.9, α_s = 4 deg, C_T/σ = 0.063 (9528)

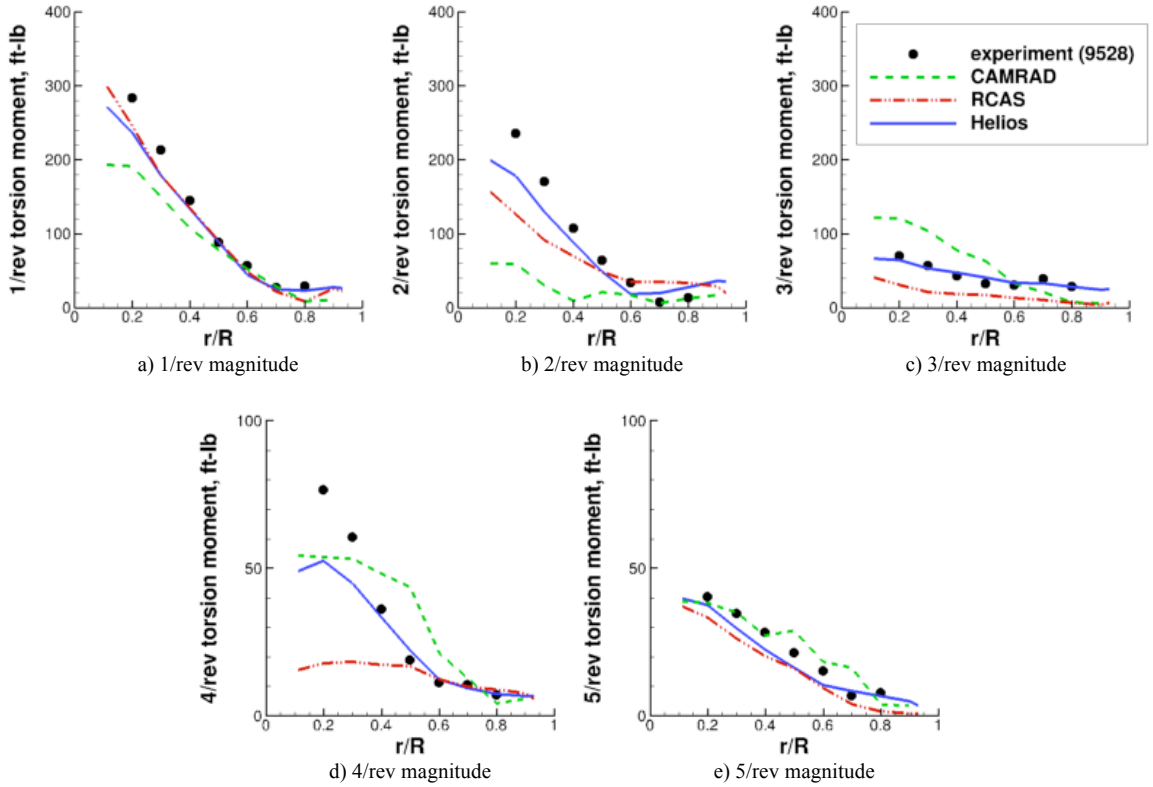

a) 1/rev magnitude b) 2/rev magnitude c) 3/rev magnitude

d) 4/rev magnitude e) 5/rev magnitude

Figure 22 Torsion moment magnitude harmonics, $\mu = 0.9$, $\alpha_s = 4$ deg, $C_T/\sigma = 0.063$ (9528)

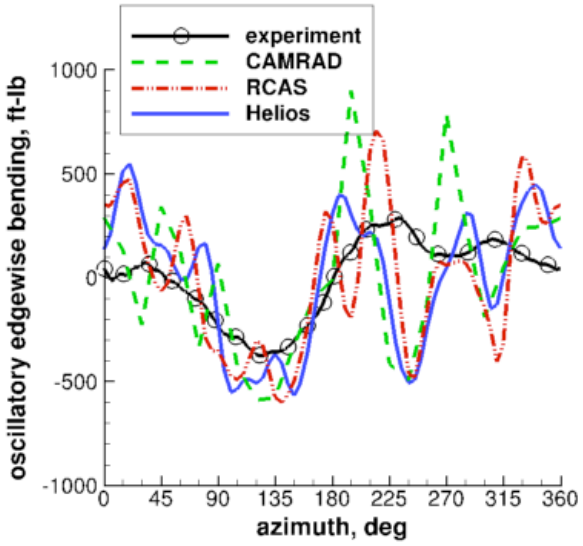

Figure 23 Oscillatory edgewise bending moments for $\mu = 0.9$, $\alpha_s = 4$ deg, $C_T/\sigma = 0.063$ (9528), r/R = 0.50

Table 3 Nominal and slowed rotor comparison

Point	M_{tip}	μ	C_T/σ	α_s	T (lbs)
6912	0.65	0.4	0.0712	0	15880
9528	0.26	0.9	0.0634	4	2280
9175s	0.26	1.0	0.0220	0	784

Comparison with Baseline Rotor (100% RPM)

It was noted in Ref. 12 that despite large differences in dimensional thrust, the UH-60A rotor at nominal RPM and low advance ratio has structural loads of the same magnitude as the slowed rotor at high advance ratio. This section investigates that progression: from a baseline case (6912: 100% RPM, $\mu = 0.4$, $C_T/\sigma = 0.071$, $\alpha_s = 0$ deg) to a slowed rotor, high advance ratio at the same C_T/σ (9528: 40% RPM, $\mu = 0.9$, $C_T/\sigma = 0.063$, $\alpha_s = 4$ deg), and finally to a low C_T/σ at the slowed RPM (9175: 40% RPM, $\mu = 1.0$, $C_T/\sigma = 0.022$, $\alpha_s = 0$ deg). These test points are summarized in Table 3. It is important to verify that the analyses can predict these trends, especially given the new technology of variable RPM rotors. Only CFD results are available for this comparison. Ref. 13 investigated the structural deformations in this vein using CFD and noted the physical mechanisms driving the trends.

Figure 24 shows the flap bending moments for these three test points. It is notable that despite all the differences in test conditions, the flap bending moments and peak-to-peak magnitudes at 50% span are of similar dimensional magnitude. In fact, the baseline rotor with a dimensional thrust of 15880 lbs is significantly more loaded than the two slowed rotor conditions at 2280 and 784 lbs, respectively, yet shows lower oscillatory flap bending, while the lowest thrust loading case shows the highest peak-to-peak loads. CFD is quite accurate in

predicting the flap bending for all three conditions, with results comparable to the advance ratio sweep (Fig. 19a). In all cases the advancing side negative flap bending phase and magnitude is exceptionally well captured. Refs. 12 and 13 showed through airloads and structural deformations that this phenomenon is due to large differential loading across the span, particularly at high advance ratio. On the retreating side the oscillations are in general agreement.

Oscillatory pitch link loads are shown in Fig. 25. There is overall good agreement in magnitude, phase and waveform trends, except that the 9528 condition appears to be poorly captured on the advancing side. Torsion moments for this test condition at r/R = 0.50 in Figs. 20 and 22 taken together would indicate that this advancing side pitch link load discrepancy is due to incorrect inboard loading, since the outboard torsion moment is so well predicted.

The advancing side loading for the baseline 100% RPM configuration (6912) is well known to be caused by tip transonic pitching moments and negative loading. For the highest advance ratio (9175) the overall advancing side elastic torsion twist level is smaller but is distributed over most of the span [13], whereas the baseline elastic torsion is limited to the tip region. This integration over the span may contribute to the similar magnitude pitch link loads. On the retreating side at high advance ratio the reversed flow and subsequent movement of the center of pressure contributes to the large loads. The two high advance ratio, slowed rotor cases have similar retreating side loads due to competing effects of shaft angle and collective, despite the thrust difference. For the baseline condition the retreating side loads are related to the torsion 4/rev response, and not a reversed flow phenomenon [12].

CONCLUSIONS

The UH-60A slowed rotor test data obtained in the US Air Force NFAC has been used for validation of comprehensive (RCAS, CAMRAD II) and CFD/CSD (Helios) analyses. This research has compared performance, airloads, and structural loads between the analyses and test data. Investigations have been performed for collective sweeps across a range of advance ratios ($\mu = 0.4–1.0$) and an advance ratio sweep at constant thrust coefficient ($C_T/\sigma = 0.063$). From the results presented, the following conclusions are drawn:

1) For performance prediction of the UH-60A, as for other rotors at high advance ratio, modeling of the shank region is critical for realistic drag prediction. CFD can do this from first principles geometry modeling, while comprehensive analyses resort to correlating with test data in order to estimate the shank drag. A drag value of the shank section is estimated from the CFD results.

2) For all analyses, rotor drag is underpredicted, while torque is overpredicted. The torque plus drag power (induced plus profile power) is reasonable, but fortuitous, given these offsetting trends.

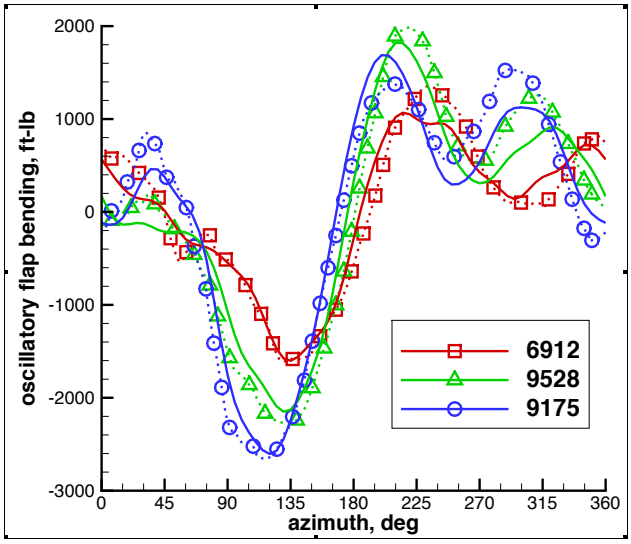

Figure 24 Oscillatory flap bending moments for baseline (6912) and slowed rotor (9528, 9175), r/R = 0.50, • • □ △ ○ • • – test, —— Helios. (See Table 3 for flight conditions)

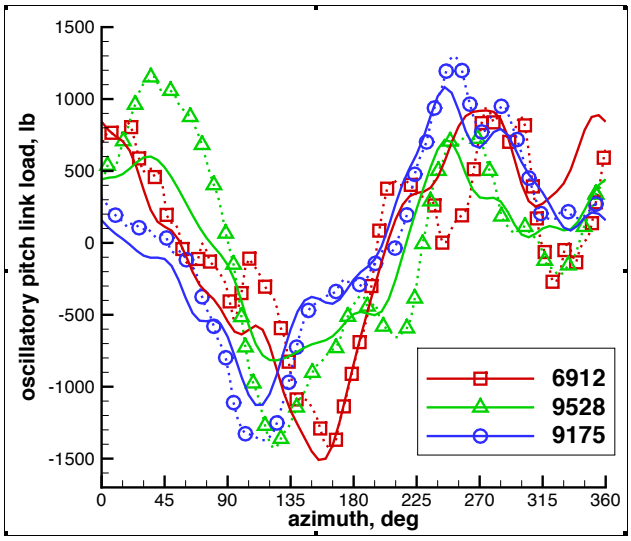

Figure 25 Oscillatory pitch link loads for baseline (6912) and slowed rotor (9528, 9175), • • □ △ ○ • • – test, —— Helios. (See Table 3 for flight conditions)

3) CFD analyses most accurately predict the drag and torque slopes and trends as a function of collective and advance ratio at zero collective. In particular, the comprehensive analyses miss the torque reduction trend toward autorotation with advance ratio.

4) Normal force airload predictions are in good agreement with the data, while pitching moment predictions are poor in the inboard reversed flow region and especially the outboard advancing side negative loading region. Further investigation of the experimental pitching moments is warranted given that oscillatory torsion loads are reasonably well predicted.

5) None of the analyses had difficulty predicting flap bending moments or the doubling in peak-to-peak magnitude with advance ratio, although CAMRAD results under-predict the peak-to-peak, while CFD is the most accurate. The vibratory flap bending is accurate in phase and magnitude. The 4/rev harmonic content is poorly captured along the span for all analyses.

6) Only the highest advance ratio vibratory torsion moments are predicted accurately in phase and magnitude, although the values at lower advance ratios are of much lower magnitude. This abrupt increase in torsion moment after $\mu = 0.7$ is accurately predicted. At the highest advance ratio, the span-wise harmonics are especially well captured by CFD, with varying degrees of accuracy from comprehensive analysis.

7) Comparing the loads from the baseline 100% RPM rotor at low advance ratio with the slowed rotor at high advance ratio, which are generally of the same magnitude, CFD results for flap bending moment and pitch link loads duplicate the data trends.

Overall, compared to previous UH-60A low advance ratio correlations in the literature and those shown here at the lowest advance ratio ($\mu = 0.4$), the current analysis predictions at high advance ratio are of equal or perhaps worse caliber than what would be expected. After all, the high advance ratio flight conditions contain no stall, low thrust, and minimal wake effects. However, the reversed flow region is a complex aeromechanics phenomenon to model. CFD stood out as being able to most accurately predict the trends with collective and advance ratio, although at a significant computational cost.

ACKNOWLEDGEMENTS

Computing resources from the DoD HPCMO and CREATE program are gratefully acknowledged. We thank the NASA Rotary Wing Project and the NFAC SRT Test Team for the data and their post-processing efforts to date. Dr. Joon Lim (AFDD) and Arsenio Dimanlig (STC Corp.) are responsible for the CFD shank geometry.

REFERENCES

1. Chase, N., "Joint Multi-Role (JMR) Technology-Enabled Capability Demonstration, CTCD," AHS Redstone Chapter Meeting, June 9, 2012.

2. Wheatley, J. B. and Hood, M. L., "Full-Scale Wind-Tunnel Tests of a PCA-2 Autogiro Rotor," NACA Report No. 515, 1935.

3. Jenkins Jr., J. L., "Wind-Tunnel Measurements on a Lifting Rotor at High Thrust Coefficients and High Tip-Speed Ratios," NASA TN D-2462, 1964.

4. McCloud, J. L., Biggers, J. C., and Stroub, R. H., "An Investigation of Full-Scale Helicopter Rotors at High Advance Ratios and Advancing Tip Mach Numbers," NASA TN D-4632, July 1968.

5. Charles, B. D., and Tanner, W. H., "Wind Tunnel Investigation of Semirigid Full-Scale Rotors Operating at High Advance Ratios," United States Army Aviation Materiel Laboratories TR 69-2, January 1969.

6. Harris, F. D., "Rotor Performance at High Advance Ratio; Theory versus Test," NASA CR 2008-215370, October 2008.

7. Floros, M. W. and Johnson, W., "Performance Analysis of the Slowed-Rotor Compound Helicopter Configuration," *Journal of the American Helicopter Society*, Vol. 54, No. 2, April 2009, pp. 22002-1-22002-12.

8. Quackenbush, T. R., Wachspress, D. A., McKillip, R. M., and Sibilia, M. J., "Experimental and Analytical Studies of Lifting Rotor Performance at High Advance Ratios," American Helicopter Society Aeromechanics Specialists' Conference, San Francisco, CA, January 2010.

9. Yeo, H., and Johnson, W., "Optimum Design of a Compound Helicopter," *Journal of Aircraft*, Vol. 46, No. 4, July-August 2009, pp. 1210-1221.

10. Ormiston, R. A., "A New Formulation for Lifting Rotor Performance Including Comparison with Full-Scale Data," American Helicopter Society 64th Annual Forum, Montreal, Canada, April 29 - May 1, 2008.

11. De Montaudouin, J., Heo, S. D., Smith, M. J., and Bauchau, O. A., "Aerodynamic and Aeroelastic Analysis of Rotors at High Advance Ratio," 36th European Rotorcraft Forum, Paris, France, September 2010.

12. Datta, A., Yeo, H., Norman, T., "Experimental Investigation and Fundamental Understanding of a Slowed UH-60A Rotor at High Advance Ratios," *Journal of the American Helicopter Society*, Vol. 58, No. 2, April 2013 , pp. 1-17.

13. Potsdam, M., Datta, A., and Jayaraman, B., "Computational Investigation and Fundamental Understanding of a Slowed UH-60A Rotor at High Advance Ratio," American Helicopter Society 68th Annual Forum, Fort Worth, TX, May 2012.

14. Yeo. H, "Investigation of UH-60A Rotor Performance and Loads at High Advance Ratios," *Journal of Aircraft*, Vol. 50, No. 2, March 2013, pp. 576-589.

15. Kottapalli, S., "Performance and Loads Correlation of a UH-60A Slowed Rotor at High Advance Ratios," American Helicopter Society Vertical Lift Aircraft Design Conference, San Francisco, CA, January 2012.

16. Ormiston, R. A. "Rotor Aerodynamic Characteristics at High Advance Ratio Relevant to Compound Rotorcraft," American Helicopter Society Vertical Lift Aircraft Design Conference, San Francisco, CA, January 2012.

17. Norman, T. R., Shinoda, P., Peterson, R. L. and Datta, A., "Full-Scale Wind Tunnel Test of The UH-60A Airloads Rotor," American Helicopter Society 67th Annual Forum, Virginia Beach, May 2011.

18. Norman, T., Peterson, R. L., Maier, T., and Yeo, H., "Evaluation of Wind Tunnel and Scaling Effects with the UH-60A Airloads Rotor," American Helicopter Society 68th Annual Forum, Fort Worth, TX, May 2011.

19. Sankaran, V., Potsdam, M., Wissink, A., Datta, A., Jayaraman, B., and Sitaraman, J., "Rotor Loads Prediction in Level and Maneuvering Flight Using Unstructured-Adaptive Cartesian CFD," American Helicopter Society 67th Annual Forum, Virginia Beach, VA, May 2011.

20. Saberi, H. A., Khoshlahjeh, M., Ormiston, R. A., and Rutkowski, M. J., "RCAS Overview and Application to Advanced Rotorcraft Problems," American Helicopter Society Fourth Decennial Specialists' Conference on Aeromechanics, San Francisco, CA, January 2004.

21. Johnson, W., "Technology Drivers in the Development of CAMRAD II," American Helicopter Society Aeromechanics Specialists' Meeting, San Francisco, CA, January 1994.

22. Yeo, H., and Johnson, W., "Prediction of Rotor Structural Loads with Comprehensive Analysis," *Journal of the American Helicopter Society*, Vol. 53, No. 2, April 2008.

23. Yeo, H., Bousman, W. G., and Johnson, W., "Performance Analysis of a Utility Helicopter with Standard and Advanced Rotor", *Journal of the American Helicopter Society*, Vol. 49, No. 3, July 2004, pp. 250–270.

24. Ormiston, R. A., "On the Definitions of Rotor and Rotorcraft Power and Performance," American Helicopter Society 69th Annual Forum, Phoenix, AZ, May 2013.

25. Vassberg, J., Tinoco, E., Mani, M., Rider, B., Zickuhr, T., Levy, D., Brodersen, O., Eisfeld, B., Crippa, S., Wahls, R., Morrison, J., Mavriplis, D., and Murayama, M., "Summary of the Fourth AIAA CFD Drag Prediction Workshop," AIAA Paper 2010-4547, AIAA 28th Applied Aerodynamics Conference, Chicago, IL, June 2010.